

Ion-Exchanging Graphenic Nanochannels for Macroscopic Osmotic Energy Harvesting

Ankit Nagar, Md Rabiul Islam, Kartheek Joshua, Tanvi Gupte, Sourav Kanti Jana, Sujan Manna, Tiju Thomas,* and Thalappil Pradeep*



Cite This: *ACS Sustainable Chem. Eng.* 2022, 10, 15082–15093



Read Online

ACCESS |



Metrics & More



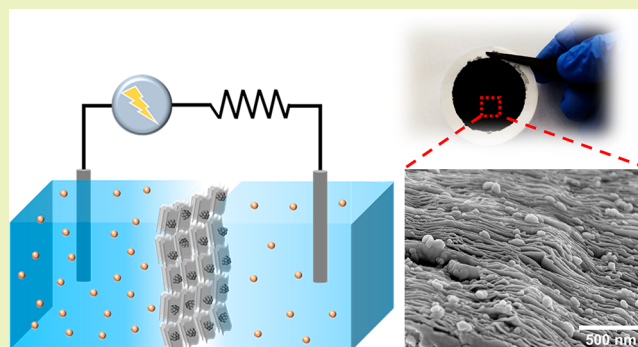
Article Recommendations



Supporting Information

ABSTRACT: The Gibbs free energy difference between seawater and river water can be tapped by selective ion transport across charged nanochannels, referred to as reverse electro dialysis (RED). However, existing single pore and micro/nanofluidic RED systems have shown poor prospects for scalability and practical implementation. Herein, we present a macroscopic RED system, utilizing a cation-selective membrane or an anion-selective membrane. The membranes comprise reduced graphene oxide (rGO) nanosheets decorated uniformly with TiO₂ nanoparticles. The nanosheets are covalently functionalized with polystyrene (PS) and subsequently linked to sulfonate or quaternary amine functional groups to obtain cation and anion selectivity, respectively. The membranes show excellent ion transport properties along with high power densities demonstrated under artificial salinity gradients. The cation-exchange membrane (CEM) delivered a power density of 448.7 mW m⁻² under a 500-fold concentration gradient, while the anion-exchange membrane (AEM) produced a substantial power output of 177.8 mW m⁻² under a similar gradient. The efficiencies ranged from 10.6% to 42.3% for CEM and from 9.7% to 46.1% in the case of AEM. Testing under varying pH conditions revealed higher power output under acidic conditions and substantial power output across the entire pH range, rendering them practically viable for sustainable energy harvesting in acidic and alkaline wastewaters.

KEYWORDS: reduced graphene oxide, electrochemistry, ion transport, osmotic energy harvesting, pH sensitivity



INTRODUCTION

Escalating energy demands and the rapid depletion of fossil fuels have necessitated the development of sustainable and renewable sources of clean energy. The osmotic energy derived from the mixing of seawater and river water is one such source that holds the potential to provide ~2 trillion watts of energy globally.¹ Currently, reverse electro dialysis (RED) is among the most promising approaches for sustainable energy harvesting. In particular, membranes comprising nanofluidic channels showing cation or anion selectivity have recently attracted attention as promising osmotic energy collectors.^{2–7} One-dimensional (1D) nanofluidic systems (single boron nitride nanotube, single-layer molybdenum disulfide nanopore, etc.) have shown promising performances as nanofluidic RED (NF-RED) devices for osmotic energy conversion.^{8,9} However, their scalability and implementation are limited by low power output due to low pore density and complex and expensive fabrication procedures. It is noteworthy that the power density extrapolated from the performance of a single pore nanotube deviates significantly from the experimental performance of an actual NF-RED system comprising arrays of such nanotubes because the measured power density is not linearly propor-

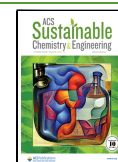
tional to the number of pores due to two primary reasons: (i) neighboring pores significantly influence the polarization and hydrodynamic flow in a pore, and (ii) an increase in number of pores results in increased interference of co-ions to hamper selective transport of counterions in the nanochannels.^{10–12} The small membrane area is compensated for by putting a stack of membranes together, which adds to the overall infrastructural cost at a large scale. Therefore, it is desirable to have a large area membrane with high power output and efficiency.

The recent emergence of membranes based on two-dimensional (2D) materials (MXenes,^{13,14} graphene,¹⁵ polymeric carbon nitride,¹⁶ kaolinite,¹⁷ titanium carbide,¹⁸ etc.) have opened avenues for scalable macroscopic energy harvesting.¹⁹ The 2D configuration significantly reduces the ion

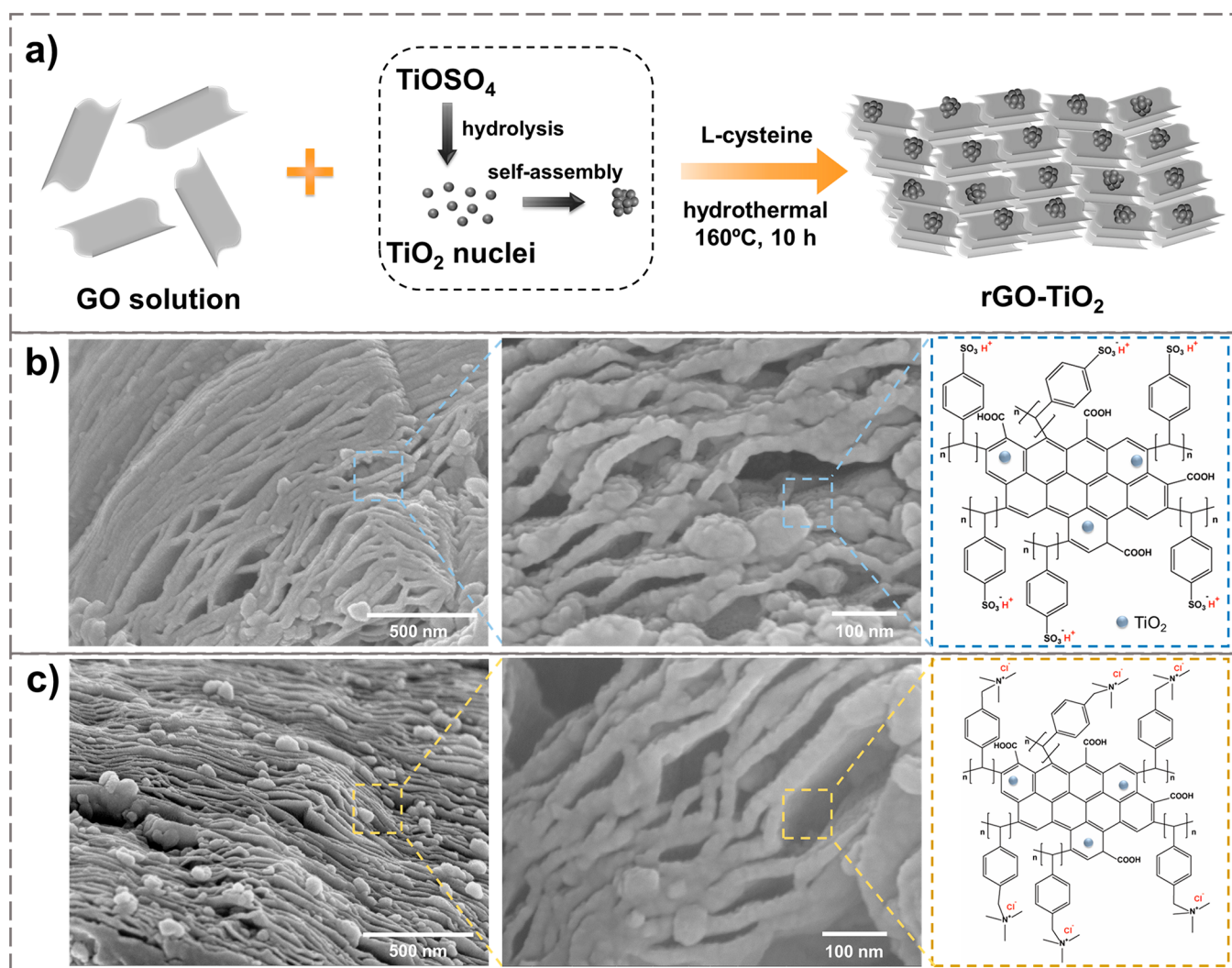
Received: July 11, 2022

Revised: October 31, 2022

Published: November 10, 2022



Scheme 1. (a) Schematic for Hydrothermal Reaction for Formation of rGO-TiO₂ Nanocomposite. (b, c) FESEM Micrographs of Cation- and Anion-Exchange Resins, Respectively, Along with Their Simplified Molecular Structures



transport resistance and offers high packing density of nanosheets without compromising the surface-determined properties in the confined spaces. An assembly of nanosheets can create uniform and continuous 2D nanochannels with interlamellar spacing close to the Debye screening length. Surface charges on these nanosheets govern the ion transport behavior across the membrane. Most intriguingly, functionalization of nanosheets can be efficiently performed in the bulk solution prior to their self-assembly, thereby bypassing the challenge of uniform functionalization of the nanochannel arrays. Such a strategy of preassembly functionalization followed by a simple bottom-up assembly process is promising for large-scale and cost-effective production of 2D material systems. The simplicity in fabrication and scalability of 2D membranes enhance their practical significance for efficient osmotic energy harvesting. The subject matter of osmotic energy harvesting has been reviewed recently, and the reader may consult the cited papers for other efforts in the area.^{20,21}

Herein, we demonstrate a macroscopic 2D membrane-based RED system wherein the membrane comprises reduced graphene oxide (rGO) nanosheets decorated with TiO₂ nanoparticles.

Graphene oxide (GO) is one of the principal derivatives of graphene, inheriting its properties such as superior mechanical and chemical robustness, atomic thickness, and oxygen-containing functionalities like carboxyl, epoxy, and hydroxyl, thereby offering possibilities of further functionalization and application.^{22–28} Moreover, GO membranes can be easily prepared at large scale using methods like vacuum filtration, coating, templating, layer-by-layer assembly, etc.²⁹ The high surface charge density and low ion transport resistance of graphene-based nanochannels also render them promising for RED-based energy conversion. Therefore, it is essential to explore 2D carbon materials in depth for large-scale clean energy applications.

TiO₂ is a renowned photocatalyst known for its nontoxicity, cost effectiveness, and long-term chemical stability.^{30,31} The presence of TiO₂ nanoparticles on the surfaces of graphene sheets increases the overall surface area, thus providing abundant nanochannels for ion transport. Also, they improve the dispersibility of graphene sheets in water, which is essential for membrane formation using vacuum filtration.

Despite having good ionic conductivities and mechanical stabilities, ion-exchange membranes with noncovalent surface modifications face several drawbacks. The functional group

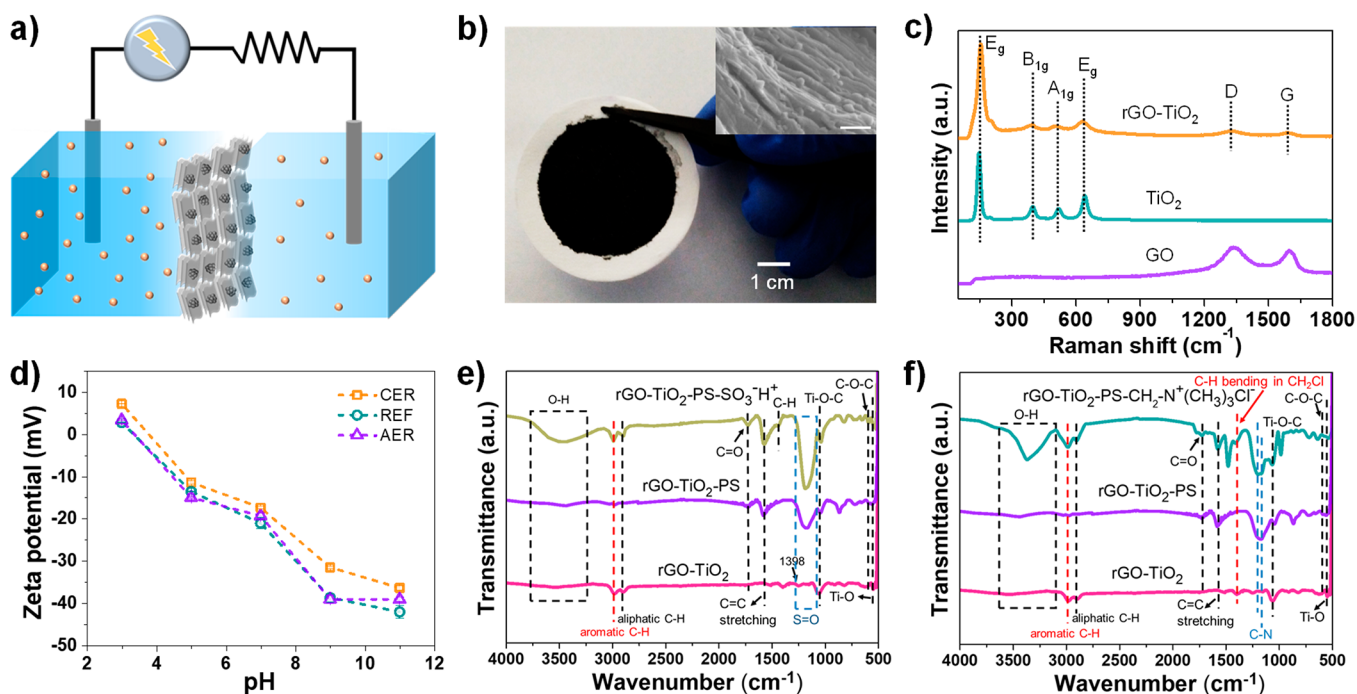


Figure 1. (a) Schematic of two-compartment setup for testing osmotic energy conversion under a salinity gradient. (b) Optical image of rGO-TiO₂ membrane. Inset shows the FESEM image of the membrane. Scale bar: 200 nm. (c) Raman spectra of GO, TiO₂, and rGO-TiO₂. (d) Zeta potentials of REF, CER, and AER with respect to pH. (e) FTIR spectra of rGO-TiO₂, rGO-TiO₂-PS, and rGO-TiO₂-PS-SO₃H. (f) FTIR spectra of rGO-TiO₂, rGO-TiO₂-PS, and rGO-TiO₂-PS-CH₂-N(CH₃)₃Cl.

withholds the risk of getting detached from the scaffold of the membrane due to weak electrostatic interaction.³² Our group has previously proven that in situ polymerization of styrene on rGO nanosheets gives materials with exceptional electroadsorption properties.³³ Therefore, in order to create robust ion-exchange membranes, the rGO-TiO₂ nanosheets (REF) were covalently linked to polystyrene (PS) prior to functionalization with the charged groups. The resulting rGO-TiO₂-PS composite was then covalently linked to sulfonate and quaternary amine groups, resulting in cation- and anion-exchange resins (CER and AER), respectively. Upon testing the energy conversion performances of the membranes under a 500-fold salinity gradient, the cation-exchange membrane (CEM) and anion-exchange membrane (AEM) revealed maximum output power densities (PD_{max}) of 448.7 and 177.8 mW m⁻², respectively. Upon further optimization of the pH conditions, maximum PD_{max} was recorded as 309.87 mW m⁻² at pH 5 for CEM and 283.50 mW m⁻² at pH 3 for AEM, under a 100-fold concentration gradient. Moreover, the ion-selective membranes showed excellent electrochemical stability during cycling and exhibited pH-sensitive ion transport. Our results demonstrate excellent potential of graphene-based covalently linked ion-exchange membranes for macroscopic RED applications to overcome the low power outputs and scalability limitations of existing ion-exchange-based RED systems.

RESULTS AND DISCUSSION

The rGO-TiO₂ nanosheets were prepared by a one-pot hydrothermal reaction between GO and titanium oxysulfate (TiOSO₄) in the presence of L-cysteine, which acted as a reducing and a cross-linking agent (details in [Materials and Methods](#)). It is known that these composite materials form by the adsorption of positively charged titanyl ions (TiO²⁺) onto

the surfaces of the negatively charged GO sheets.^{34,35} During the hydrothermal reaction, hydrolyses of TiO²⁺ ions result in the formation of TiO₂ nuclei which grow to form surface-anchored nanoparticles, while GO reduces to rGO. The π - π interaction between the rGO sheets and the coexistence of electrostatic interaction and hydrogen bonding among L-cysteine and rGO contribute toward the formation of an integrated lamellar structure. Lower concentrations of the Ti precursor do not result in any aggregation of TiO₂ nanoparticles; however, at larger concentrations, TiO₂ particles self-assemble into nanoaggregates.³⁶ The field emission scanning electron microscopy (FESEM) micrographs of CER and AER demonstrated arrays of nanosheets uniformly intercalated with nanoparticles ([Scheme 1](#)).

Further, the resins were self-assembled using vacuum filtration on a grade 42 Whatman paper support, and the resulting ion-exchange membranes were tested for ion transport and energy conversion ([Figure 1a, b](#); [Figure S1](#)). The test membranes were individually placed at the junction of a two-compartment electrochemical cell to evaluate their energy conversion performance ([Figure 1a](#)). Two Ag/AgCl electrodes were placed in either cell and connected to an external load resistance and a pico-ammeter. The morphology of the membrane reveals the presence of lamellar structures with uniformly anchored TiO₂ nanoparticles ([Scheme 1](#), [Figure 1b](#) inset, and [Figure S2](#)).

The Raman spectra of GO, TiO₂, and rGO-TiO₂ nanocomposites are shown in [Figure 1c](#). The Raman spectrum of GO depicted its characteristic D- and G-band at 1353 and 1602 cm⁻¹, respectively. The D-band was attributed to sp³ defect-induced disorders on graphene sheets, and the G-band was ascribed to in-plane vibrations of sp² hybridized carbons and scattering of E_{2g} phonons. It is evident from the spectra that conversion of GO to rGO results in downshifting of the

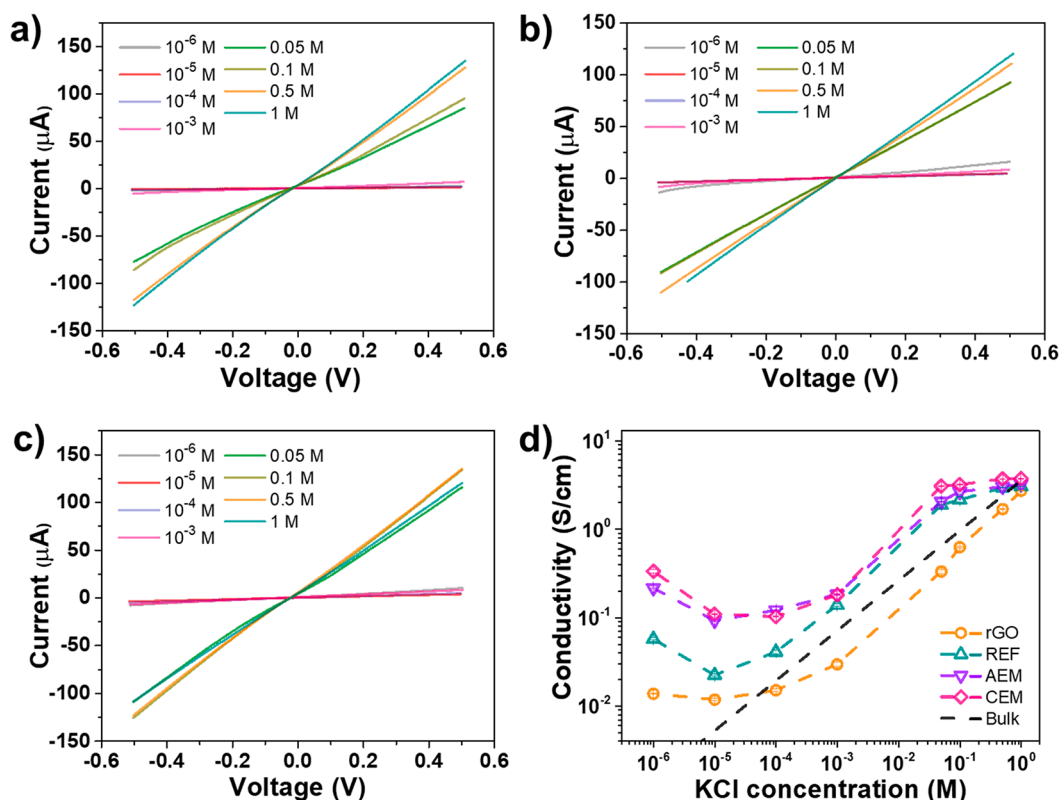


Figure 2. I–V characteristics of the membranes: (a) REF, (b) CEM, and (c) AEM. (d) Ionic conductivities of the membranes over a range of KCl concentrations (10^{-6} to 1 M), which deviates significantly from the bulk conductivity (dashed line) of the electrolyte. All measurements were performed at 300 K.

D-band peak from 1339 to 1327 cm^{-1} and G-band peak from 1602 to 1593 cm^{-1} . This confirmed successful hydrothermal reduction of GO to rGO.³⁷ The shift of the D-band could possibly be due to multiple foldings in the rGO-TiO₂ nanosheets, formed during the hydrothermal reduction (Figure S3). Broad peaks in the case of the rGO-TiO₂ nanocomposite were a result of stacking of multiple layers of rGO sheets due to the presence of a fewer number of oxide functional groups after reduction of the exfoliated GO, thereby causing structural disorder. In addition, the E_g , B_{1g} , A_{1g} and E_g modes implied the existence of the anatase phase in the nanocomposite, also consistent with XRD results (Figure S4).

Surface charges of the resins were confirmed by zeta potential measurements (Figure 1d). Zeta potentials of REF, CER, and AER became increasingly negative as pH was varied from 3 to 11. The negative zeta potential was attributed to the oxygen-containing functional groups such as $-\text{COOH}$ and $-\text{OH}$.^{38,39} The variation in zeta potential with pH confirmed the strong dependence of surface charges on pH. Since sulfonate and quaternary amine are strong acid and strong base resins, respectively, they always undergo complete dissociation in an aqueous medium irrespective of pH and have on role in the pH-dependent zeta potential variation.

Figure 1e and f represents Fourier transform infrared (FT-IR) spectra for sulfonate and quaternary ammonium-functionalized rGO-TiO₂ nanocomposites alongside rGO-TiO₂ and rGO-TiO₂-PS, prior to resin functionalization. The vibrational features confirmed the covalent linkage between rGO and polystyrene (PS), along with the covalently linked positively and negatively charged functionalities. The FT-IR spectrum of CER (Figure 1e) showed a broad peak in the range of 3421–

3561 cm^{-1} , corresponding to O–H stretching. This feature could be attributed to the adsorbed humidity from the surroundings or the presence of NaOH used during the styrene polymerization process. Peaks at 2979 and 2899 cm^{-1} were assigned to the asymmetric and symmetric stretching frequencies of aliphatic C–H, respectively. Also, the peaks at 2988, 1579, and 1438 cm^{-1} were assigned to aromatic C–H stretching, C=C stretching, and C–H bending, respectively. Another peak at ~ 1719 cm^{-1} is due to C=O stretching of the carboxyl group. All the aforementioned peaks were also observed in cases of rGO-TiO₂-PS and rGO-TiO₂. The CER spectrum had a peak at 1180 cm^{-1} which confirmed the presence of the S=O bond of the sulfonate group. The presence of Ti–O–C bonds in all spectra was confirmed by the peak at 1054 cm^{-1} . In addition, the peak at 1438 cm^{-1} confirmed C–H vibrations due to chloromethylation. The FTIR spectrum of AER (Figure 1f) showed peaks at 2982 and 2899 cm^{-1} for aromatic and aliphatic C–H, respectively. The peak at 1573 cm^{-1} depicted C=C stretching. Post amination, peaks at 1197 and 1161 cm^{-1} were C–N stretching frequencies of the quaternary amine group. The broad features in 600–800 cm^{-1} and the sharp feature in 1036–1060 cm^{-1} across all spectra were ascribed to the presence of Ti–O–Ti and Ti–O–C stretching vibrations.⁴⁰

The surface areas and pore sizes of the rGO-TiO₂ particles are critical in determining the membrane's ion transport and energy conversion properties. We performed Brunauer–Emmett–Teller (BET) surface area measurements on three rGO-TiO₂ composites with varying TiO₂ loadings from (0%–99% w/w). We found that an increase in TiO₂ loading leads to an increase in the specific surface area (Table S1). A larger

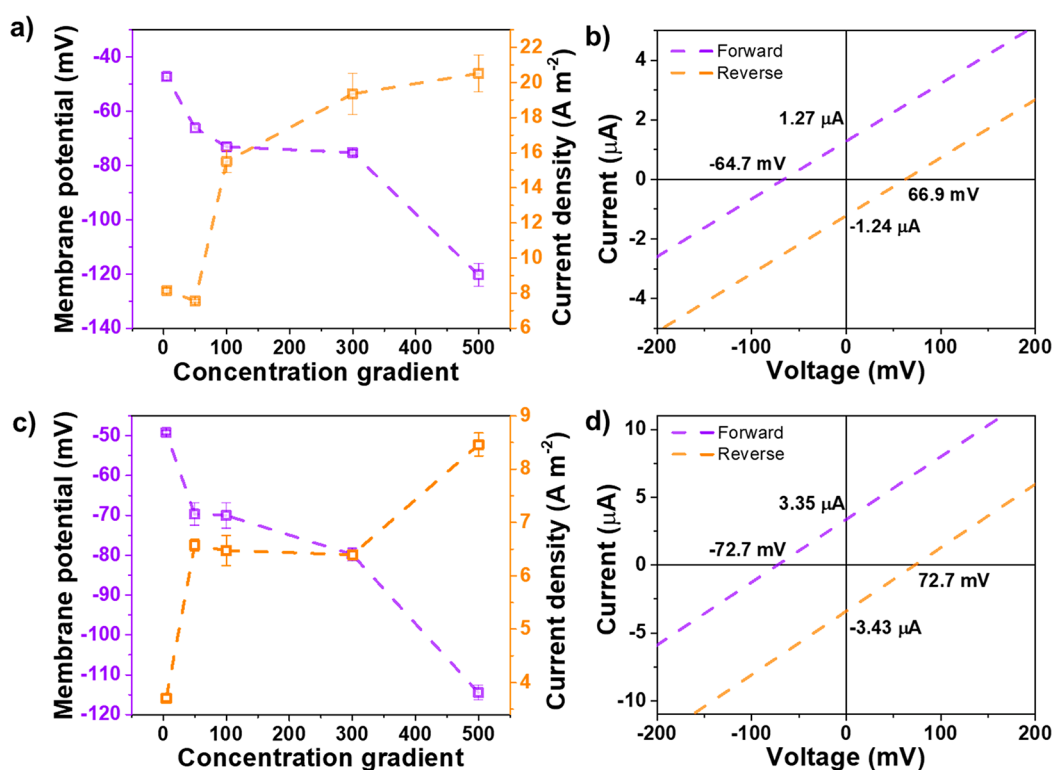


Figure 3. Membrane potential (V_{oc}) and current density (J_{sc}) represented as a function of concentration gradient for (a) CEM and (c) AEM. The bidirectional ion-transport behaviors of CEM and AEM are evident at a concentration gradient of 50 (0.01 M/0.5 M) from the I–V curves shown in (b) and (d), respectively.

surface area indicates the presence of abundant nanochannels.⁴¹ Therefore, TiO₂ loading was kept at 99% (w/w) in the rGO-TiO₂ nanocomposite. All composites were found to be mesoporous in nature with pore sizes in the range of 2–10 nm (Figures S5, S6). The role of TiO₂ is also apparent from the improved dispersibility of the rGO-TiO₂ sheets in an aqueous medium, in comparison to rGO (Figures S7, S8).

The rGO-TiO₂ particles were vacuum filtered through a grade 42 Whatman paper support to create a membrane which was subsequently fixed at the junction of the two-compartment electrochemical cell (Figure 1a). A neutral probe molecule, ovalbumin, was chosen to permeate across the membrane to check for the presence of any macroscopic defects. However, the molecule failed to permeate, indicating that the prepared membrane was defect free (Figure S9).

Transmembrane Ion Transport. To investigate the ion transport characteristics, the membranes were individually placed at the junction of a homemade two-compartment electrochemical cell (see Materials and Methods). KCl was selected as the test electrolyte due to identical electrophoretic mobilities of K⁺ and Cl⁻ ions. The current–voltage (I–V) characteristics for the membranes were recorded under a series of KCl concentrations varying from 10⁻⁶ to 1 M. Figure 2a–c shows I–V curves for REF, CEM, and AEM, respectively. All curves show linear ohmic behavior. The conductance vs concentration curves for the three membranes exhibit two distinct behaviors across the entire concentration range (Figure 2d). In the high concentration range (>10⁻³ M), conductance follows the bulk rule and exhibits linear behavior. In the low concentration regime (<10⁻³ M), the curves gradually deviate from the bulk electrolyte's linear curve. At lower concentrations, the Debye length significantly increases, and therefore,

surface charges dominantly govern ion transport across the nanochannels, thereby causing a deviation from linearity.^{42–46} Moreover, the rGO-TiO₂ membrane has substantially better ionic conductivity compared to the rGO membrane across the entire concentration range, suggesting that the presence of TiO₂ nanoparticles enhances the overall ion transport. It is also evident from the conductivity curves that the conductances of CEMs and AEMs are nearly the same across the entire concentration range and about an order of magnitude higher than the conductance of REF in the low concentration range (Figure 2d). This implies that the introduction of ion-selective functional groups on the rGO-TiO₂ nanosheets significantly enhances their ionic conductivity and permselectivity.

It is also observed that for all the membranes, REF, AEM, and CEM, conductivities do not change significantly beyond 0.1 M KCl concentration. This is likely due to osmotic deswelling of the membrane at higher salt concentration, which reduces the available volume for ion transport within the membrane.⁴⁷

Concentration Gradient-Driven Transport. Further, the ion transport properties of CEM and AEM were utilized for extracting artificial salinity gradient energy by placing a test membrane at the junction of two compartments containing the NaCl electrolyte of different concentrations.^{48,49} The concentration in one compartment was kept fixed at 0.01 M, and the concentration in the other compartment was varied from 0.05 to 5 M. The cation- or anion-selective nature of the membranes allows selective permeation of counterions (Figure S10), thereby converting the chemical potential gradient into a finite ion diffusion current.^{50–52} The energy conversion performance was characterized by the I–V curves. The short-circuit current (I_{sc}) and open-circuit voltage (V_{oc}) were

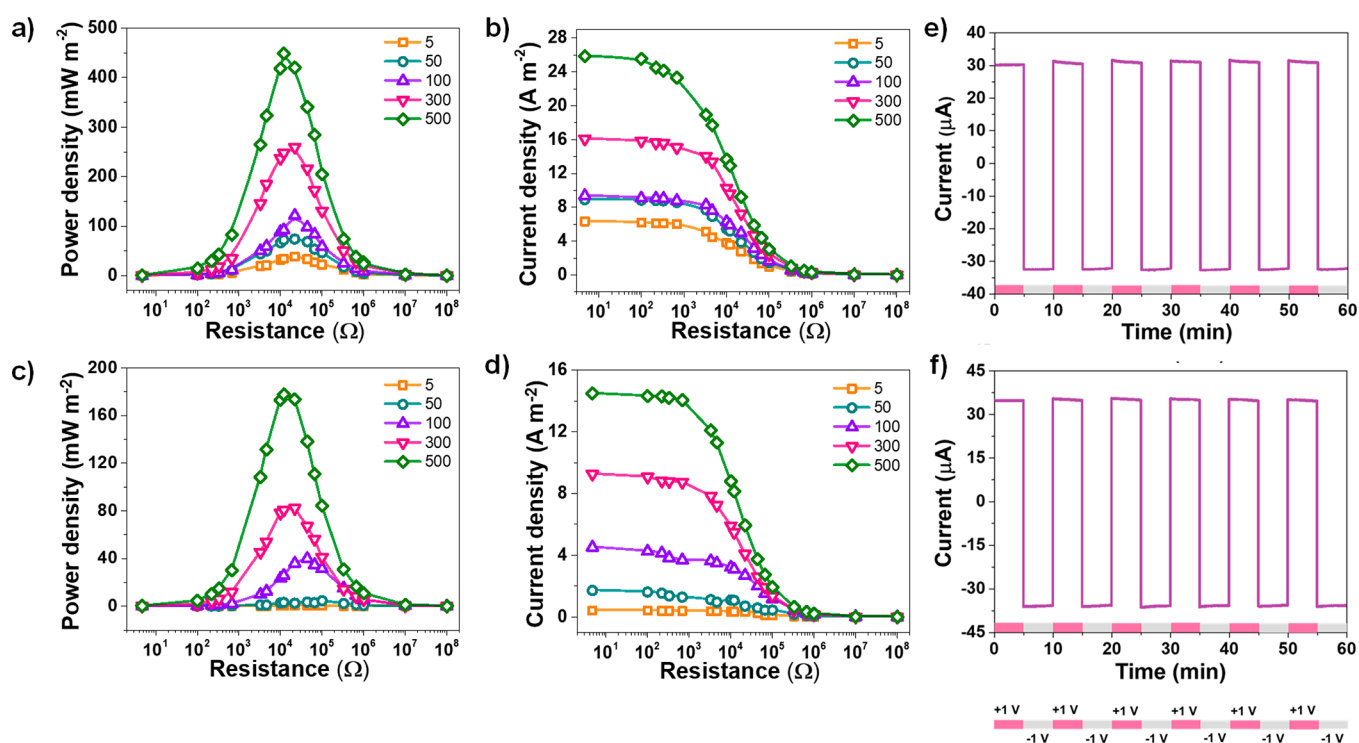


Figure 4. Energy harvesting performance. (a, c) Power densities of CEM and AEM, respectively, as a function of externally applied load resistance. Power output reaches a maximum at a certain moderate load. (b, d) Corresponding current densities of CEM and AEM, respectively. (e) Cyclic stabilities of the membranes were studied using a current–time curve. External biases of +1 V and –1 V were alternately applied, each for a 5 min period. Curve in (e) for CEM and (f) for AEM.

derived from the intercepts of the I–V curves measured at varied concentration gradients, ranging from 5 to 500. In the case of CEM, the membrane potential ranged from –47.4 mV under a 5-fold gradient up to –120.5 mV under a 500-fold gradient (Figure 3a). Similarly, the current density increased from 8.12 to 20.50 A m⁻² when the gradient was varied from 5-fold to 500-fold, respectively (Figure 3c). On the contrary, the membrane potential for AEM was measured to be –49.2 mV under a 5-fold gradient and a maximum of –114.5 mV under a 500-fold gradient. The current density ranged from 3.71 to 8.46 A m⁻² at a 500-fold gradient. Consistent increases in both V_{oc} and J_{sc} were observed with increases in concentration gradients for both CEM and AEM (Tables S2, S3). Figure 3b and d shows that on reversing the concentration gradient V_{oc} and I_{sc} do not change significantly, confirming that there is no preferred direction for ion transport.

Further, ion selectivities of the membranes were evaluated by the ion transference number t_n using the following equation: $t_n = 0.5 (1 + V_{os}/V_{redox})$; t_+ for CEM and t_- for AEM. The transference number equals 1 for a perfectly ion selective system and 0.5 for a nonselective system. In the equation above, V_{os} is the osmotic potential, and V_{redox} is the potential drop at the electrode–solution interface. The osmotic potential can be calculated by subtracting the contribution of redox potential from the open circuit potential, i.e., $V_{os} = V_{oc} - V_{redox}$ (Figure S11). The transference number for CEM, t_+ , varies from 0.73 to 0.96, indicating a high charge selectivity (Table S2). AEM shows similar selectivity as t_- varies from 0.72 to 0.98 (Table S3). The energy efficiency for CEM ranges from 10.6% at 100-fold and 300-fold gradients and up to 42.3% at a 5-fold gradient. For AEM, the efficiency ranges from 9.6% at a 100-fold gradient and up to 46.1% at 5-

fold gradient. Therefore, both CEM and AEM promise high-cation selectivities and excellent energy efficiencies in a macroscopic RED system.

Osmotic Energy Harvesting. A two-compartment setup was used to investigate the energy harvesting behaviors of the CEM and AEM membranes. Artificial salinity gradients were created using the NaCl electrolyte. The membranes were tested under five concentration gradients ranging from 5 to 500. The concentration on one side was kept fixed at 0.01 M and varied on the other side from 0.05 to 5 M. Each measurement was performed using fresh solutions.

Irrespective of the membrane type (CEM or AEM), it was observed that current densities decreased systematically with an increase in the load resistance (Figure 4b, d). Output power density was calculated using the equation $P_L = (I^2 \times R_L)/A$, where P_L is the areal power density, I the measured current in the external circuit, R_L the externally applied load, and A the actual membrane area available for ion transport. For a fixed concentration gradient, the diffusion current decreases with an increase in the external load. This was true for both CEM and AEM under all gradients (Figure 4b, d). Moreover, the diffusion current increases with an increase in the concentration gradient. The aforementioned equation for power density implies that power output will be maximum upon application of a certain moderate load. The CEM showed PD_{max} values of nearly 448.6, 259.4, 121.5, 74.2, and 38.2 mW m⁻², and AEM delivered PD_{max} of 177.8, 82.1, 39.9, 3.4, and 0.7 mW m⁻², under artificial salinity gradients of 500, 300, 100, 50, and 5, respectively (Figure 4a, c). Due to higher power densities obtained in the case of CEM, we decided to further investigate its ion transport for different electrolytes containing chloride ions, keeping a constant concentration

gradient of 50 (0.01 M/0.5 M) to assess the membrane performance under varied practical working conditions. The obtained PD_{\max} values for LiCl, NaCl, and KCl electrolytes were 460.38, 223.2, and 120.3 $mW m^{-2}$, respectively (Figure S12). Therefore, the ion current follows the following order: LiCl > NaCl > KCl. On the contrary, hydrated diameters of the aforementioned ions follow the opposite trend: Li^+ (7.6 Å) > Na^+ (7.2 Å) > K^+ (6.6 Å). Therefore, the governing factor for ion transport must be the binding affinity of the sulfonate group to test ions, which follows as K^+ > Na^+ > Li^+ . A higher binding affinity and smaller size allows easier condensation of cation–sulfonate pairs, thereby preventing dissociation for fast ion transport.⁵³

Cyclic stabilities of the membranes were studied by applying an external bias of +1/−1 V alternately and subsequently recording the current–time characteristics for both the membranes (Figure 4e, f). The duration for each cycle was 5 min. A total of 12 cycles was performed for a duration of 60 min. The positive and negative currents at the applied biases remain nearly constant across the entire duration indicating remarkably stable ion transports for both CEM and AEM. Further, the output power density was observed to remain stable in the case of CEM for a period of 15 days under a 500-fold gradient (Figure S13).

In Figure 5 and Table S4, we compare the energy harvesting performance of CEM alongside the three kinds of membrane-

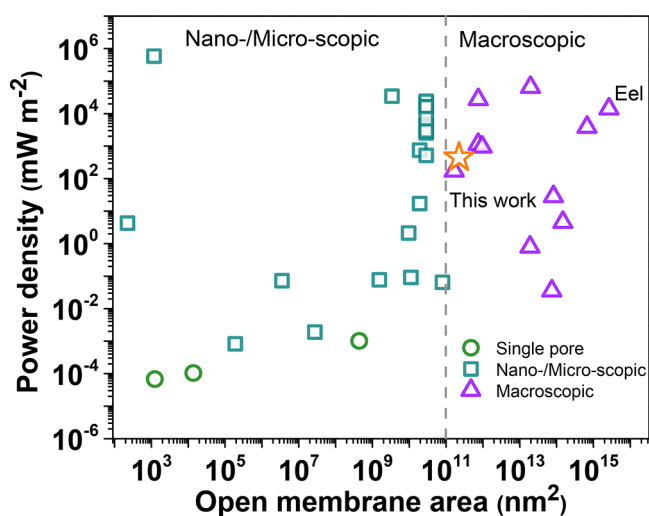


Figure 5. Osmotic energy conversion performance of state-of-the-art RED devices alongside this work (cation-exchange membrane). Power densities were calculated by normalizing the obtained power with the total active membrane area used for ion transport. The threshold for distinguishing the nano/microscopic systems from the macroscopic systems is $10^{11} nm^2$ (or $0.1 mm^2$).

based single-stage RED systems: single pore, nano/microscopic, and other macroscopic devices. For the sake of simplicity, we only show CEM, since it offers slightly better performance and efficiency compared to AEM at a 500-fold gradient. The three types of devices are distinguished based on the active membrane area utilized for ion transport. The majority of the data obtained for comparison in Figure 5 was at a 1000-fold concentration gradient, while CEM's performance used for comparison was at a 500-fold gradient (Table S3). As evident from the figure, electric eels outperform all artificial RED systems in the context of large-area power conversion.

Several 2D/3D macroscopic systems such as MXene-GO composite,⁵⁴ MXene-bacterial cellulose composite,⁵⁵ metal–organic frameworks,⁵⁶ covalent–organic frameworks,⁵⁶ etc., have higher power densities in comparison to this work, as shown in Figure 5. However, such reports lack discussion on ion transference number or energy efficiency at the highest recorded power density. Also, some of the systems highlight power densities corresponding to stacks of several membranes, while power density in this work was generated from a single membrane in a two-compartment electrochemical cell.

While a few single pore systems generate higher power densities in comparison to a live eel, they require sophisticated methods to enhance the number of pores to achieve substantial power for practical use. On the contrary, graphene-based nanochannels presented in this work do not require precise nanofabrication. The membrane areas of CEM and AEM used in this study are $\sim 0.22 mm^2$, which are apt for practical purposes, in comparison to the sub- μm^2 active area of other reported membranes. Moreover, small testing areas do not precisely project the performance of a large-scale RED system as power density does not vary linearly with the membrane area. An extension of this work for further optimization of membrane thicknesses and their degree of functionalization could help approach the performance of a live electric eel.

Ion Transport Model. To understand the molecular interactions and confirm that permselectivities of the membranes play roles behind excellent ion transport, we performed molecular dynamic (MD) simulations on the CEM. Details of the method used are provided in Materials and Methods. As a simplified model, graphene sheets of $5 nm^2$ areas were generated and functionalized with epoxy, hydroxyl, and carboxyl groups (Figure S14a). The sheets were further functionalized with $-SO_3H$ to create a simplified mimic of the experimentally synthesized material (Figure S14b). After functionalization, sheets were replicated with a 1.5 nm interlayer separation. A total of four replica layers were created, resulting in three nanochannels.

To understand the interaction of Na^+ and Cl^- ions with the $-SO_3H$ and oxygen-containing groups of rGO, we focused on a single nanochannel between two functionalized rGO sheets. Three NaCl electrolyte concentrations of 0.5, 1.0, and 1.5 M were chosen to permeate across the nanochannel with the application of an external pressure. To understand interactions between the ions and the functional groups, the proximities of Na^+ and Cl^- ions were monitored during the simulation to scan for the presence of any sulfur and oxygen atoms in their vicinity. Figure 6a depicts an example of the 1.0 M system with its initial and final states. Figure S15 shows such representations at all concentrations. The interactions were analyzed by calculating the radial distribution function (RDF), $g(r)$. For the 0.5 M concentration, the flat RDF profile in case of Cl^- -S indicated the absence of any Cl^- -S interaction (Figure 6b). We conclude that Cl^- ions do not interact with sulfonate groups at this condition. Similarly, the Cl^- -S interaction begins at 8.0 and 7.0 Å for 1.0 and 1.5 M concentrations, respectively. This suggests negligible interactions between sulfonate groups and chloride ions during electrolyte permeation. On the other hand, Cl^- ions significantly interact with the oxygen atoms on the rGO sheet, indicated by shorter interaction distances (Figure 6c). At 0.5 M, Cl^- -O interaction starts at 3.0 Å, and a highly stable confirmation and interaction is observed at 4 Å, suggested by the peak. Similarly, a Cl^- -O interaction is observed at 3 and 3.5 Å for 1.0 and 1.5 M, respectively. These

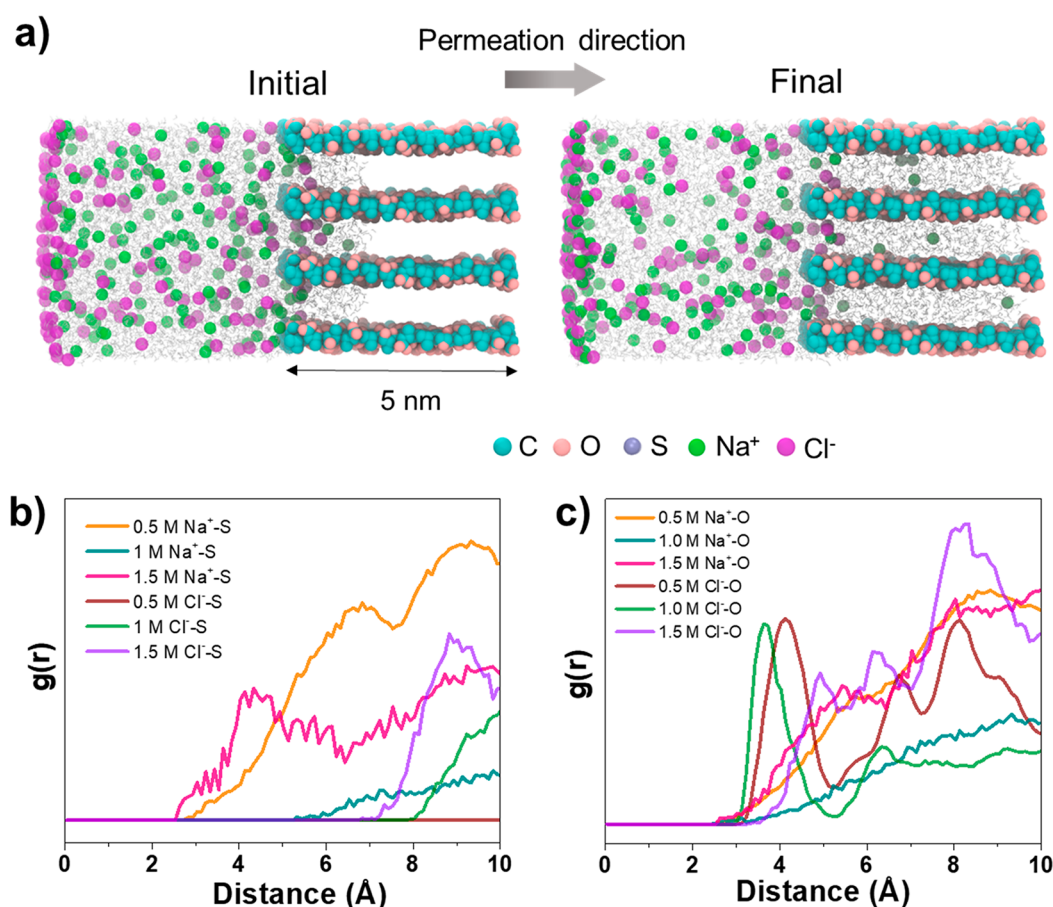


Figure 6. (a) Representations of initial and final conformations of the ion-permeation simulation performed at 1.0 M concentration. The glassy-colored water molecules are also shown. (b, c) Atom density profiles, $g(r)$, of NaCl electrolyte diffusing through a sulfonate-functionalized graphene oxide nanochannel at 300 K for 0.5, 1.0, and 1.5 M, electrolyte concentrations.

collectively suggest that Cl⁻ ions preferentially interact with oxygen-containing groups and are rejected by the sulfonate groups.

At a 0.5 M concentration, Na⁺-S and Na⁺-O interactions begin at 2.8 and 2.5 Å, respectively (Figure 6c). Also, stable Na⁺-S interactions are observed at 6.8 Å, as indicated by the peak in the RDF curve, which imply that sulfur atoms cause Na⁺ ions to stabilize within the channel. In the case of a 1.0 M concentration, the Na⁺-O interaction begins at 2.5 Å, while Na⁺-S at 5.2 Å. At a 1.5 M concentration, the Na⁺-O interaction begins at 2.5 Å, and most stable conformations are found at 5.5 Å. The radial distribution interaction values are provided in Table S5. Negligible Cl⁻-S interactions across all concentrations, and stable interactions between Cl⁻-O, Na⁺-O, and Na⁺-S, as suggested by the local maxima in RDF curves, verify the permselective behaviors of the sulfonated nanochannels.

pH Sensitive Ion Transport and Energy Conversion.

From the results of zeta potential with respect to pH (Figure 1d), it was observed that the surface charge densities of the functionalized nanosheets increase consistently with an increase in pH from 3 to 11. Since nanoscale ion transport is highly dependent on the surface charge densities of the nanochannels, transport is expected to be highly pH sensitive. To confirm this, we carried out the energy harvesting experiments with varying pH under a 100-fold artificial salinity gradient. Electrolytes in both the compartments were maintained at the same pH. PD_{max} values for both CEM and

AEM were observed to be higher in an acidic environment. CEM and AEM recorded highest PD_{max} values of 309.87 and 283.50 mW m⁻² at pH of 5 and 3, respectively (Figure 7a, c). Higher ion currents in acidic conditions imply excellent proton transport abilities of CEM and AEM (Figure 7b, d). It is known that strong-acid cation-exchange resin and strong-base anion-exchange resin always undergo complete dissociation independent of pH. Therefore, sulfonate- and quaternary amine-functionalities cannot show pH responsivity. On the contrary, weak-acid resins containing carboxylic acid groups have high affinity for H⁺ ions. Therefore, they are prone to protonation in acidic conditions, thereby losing their ionic state. On the contrary, carboxylic acid groups remain ionized in alkaline conditions. Therefore, the graphene nanosheets are inherently pH sensitive. In basic conditions, the ionized carboxylic acid groups on nanosheets restrict the movement of anions within the nanochannel, thereby resulting in lower ion current in alkaline pH. In acidic conditions, the protonated carboxylic acid groups offer lower resistance to the movement of protons across the channels, thereby producing higher ion current in acidic pH.

Aspects of Sustainability. It is known that RED is a sustainable methodology for harvesting blue energy. Upon further optimization of membrane thickness and active area, and by putting together a stack of membranes, it is possible that osmotic energy harvesting through this method becomes practically viable.

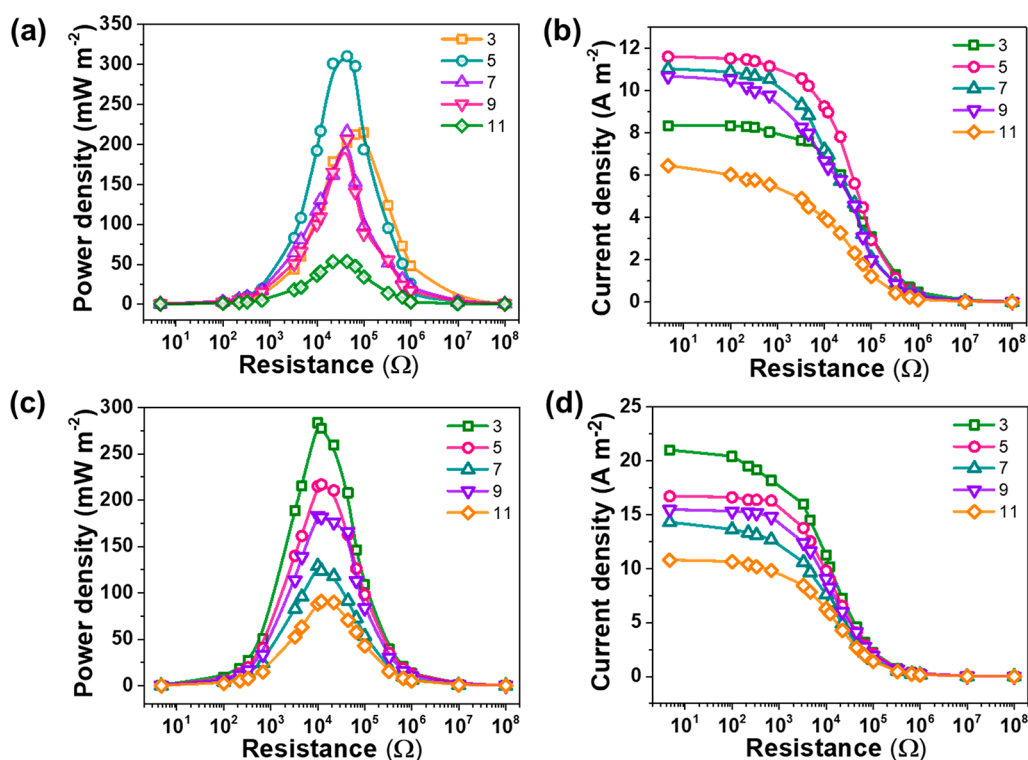


Figure 7. pH-sensitive ion transport. Power densities of CEM and AEM (a, c) and their respective current densities (b, d) measured under varying pH conditions (3–11).

CONCLUSION

In conclusion, we fabricated an array of wrinkled rGO-TiO₂ nanosheets that were covalently linked to sulfonate or quaternary amine functional groups to create cation- and anion-exchange resins. The membranes prepared from these resins show ion selectivity confirmed from their ionic conductivity curves. The highest ever macroscopic osmotic energy conversion performance was obtained when the membranes were tested under artificial salinity gradients. At a concentration gradient of 500, the cation-exchange membrane (CEM) produces a power density as high as 448.7 mW m⁻², while the anion-exchange membrane could deliver a maximum power density of 177.9 mW m⁻². The robust functionalization of nanochannels assured through covalently linked ion-selective groups also delivered an improved power density for CEM in the case of a LiCl electrolyte. The membranes were also found susceptible to pH changes, showing excellent proton transport abilities. The tunable nanochannel sizes and surface charge densities, pH responsiveness, and functional robustness render the materials promising for sustainable energy harvesting.

MATERIALS AND METHODS

Chemicals. Flakes of natural graphite were purchased from Active Carbon India Pvt. Ltd. Sulfuric acid (H₂SO₄, 95%–98%) and hydrochloric acid (HCl, 36%) were obtained from Rankem Chemicals Pvt. Ltd. The styrene monomer (C₈H₈) was procured from Avra Synthesis Pvt. Ltd. Nitric acid (HNO₃, 65%–68%) and potassium chloride (KCl, 99%) were obtained from Merck, India. Lithium chloride anhydrous (LiCl, 99%) was obtained from Sisco Research Laboratories Pvt. Ltd.

Characterization. FE-SEM images were captured using a Thermo Scientific Verios G4 UC SEM. IR spectra of rGO-TiO₂ and related functionalized composites were measured by a PerkinElmer FT-IR

spectrometer. Samples were freeze-dried using an Eyla freeze-dryer (Model No: FDU-1200). Powder XRD data were measured using a Bruker D8 Advance X-ray diffractometer with Cu K α as the source of irradiation ($h\nu = 8047.8$ eV).

Resin Preparation and Membrane Fabrication. The rGO-TiO₂ powdered material was prepared by carrying out a hydrothermal reaction between the TiOSO₄ solution (1.0 g) and GO suspension (1 mL) in the presence of L-cysteine. The mixture of these precursors was kept in an autoclave for 12 h at 160 °C. Post reaction, the product was thoroughly washed in a 1:1 water–methanol mixture.

Before polystyrene functionalization, the prepared rGO-TiO₂ powder (100 mg), styrene monomer (15 mg), and divinylbenzene (1.5 mg) were mixed in deionized (di) water (25 mL). The polymerization process was performed in atmosphere by purging N₂ gas. Under constant stirring, K₂S₂O₈ (320 mg) was added to the mixture. Stirring was carried out for another 30 min at room temperature. The temperature of the mixture was then increased to 70 °C and maintained for 1 h. After 1 h, the temperature was increased to 90 °C and maintained under stirring for the next 12 h. After completion, the product was washed two to three times with di water and kept in a hot air oven at 90 °C for drying. For sulfonation, the prepared rGO-TiO₂-PS powder was suspended in H₂SO₄ (4 M) for 24 h at 100 °C under constant stirring. The product was later washed in a 1:1 water–methanol mixture.

For AER, anion-exchange rGO-TiO₂-PS was functionalized with chloromethyl groups by the Friedel–Craft alkylation reaction. Next, the resulting composite (1 g) was added to a mixture of chloromethyl methyl ether (3 mL) and di water (10 mL). After stirring at room temperature (RT) for 2 h, ZnCl₂ (380 mg) was added and stirring was continued for another 12 h at ~35 °C. The chloromethylated product was rinsed in acetone and dried at 65 °C overnight. It was then allowed to swell in 1,2-dichloromethane for 2 h. Further, trimethylamine hydrochloride (1 g) was added to the mixture and kept for stirring at RT for 6 h. The final chloro-aminated resin (rGO-TiO₂-PS-CH₂-N⁺(CH₃)₃Cl⁻) was dried in an oven at 65 °C. Membranes (CEM and AEM) were prepared by vacuum filtration

of the obtained corresponding powdered materials through grade 42 Whatman filter paper.

Electrical Measurements. Ionic conductivity measurements were performed using a CH Instruments electrochemical analyzer (CH 600A). The test membrane was mounted at the junction of a two-compartment cell, each a 40 mL volume. The conductivity and energy conversion experiments were performed by placing an Ag/AgCl electrode in either compartment. For the energy conversion experiments, the electrodes were connected to a picoammeter (Keithley 6485). For the pH-dependent studies, the pH values of the electrolytes were adjusted using stock solutions. Here, 0.01 M stock solutions of NaOH and HCl were used for obtaining alkaline or acidic conditions, respectively. Fresh electrolytes were used for all measurements.

MD Simulations. Graphene sheets of 5 nm² areas were generated using the GOPY package.⁵⁷ The sheets were further functionalized with -SO₃H to create cation-exchange nanochannels. MD simulation-related parameters and charges of the carboxyl, epoxy, and hydroxyl groups were adopted from a computational study where authors had conducted extensive studies on the biomolecular interactions with GO, rGO, and graphene sheets.⁵⁸ Parameters for -SO₃H were obtained from GAFF through the antechamber program of Ambertools21.^{59–61} MD simulations were performed with GROMACS version 2021.2. Force field parameters for GO were taken from a previous study and implemented in AMBER99.⁵⁸ The TIP3P water model was used to construct the water box. All carbon atoms constituting the GO sheets were positionally restrained (1000 kJ mol⁻¹ nm⁻²) throughout the simulation for all the systems to maintain an intersheet separation of 1.5 nm. The LINCS algorithm was used to constrain H-bonds, and periodic boundary conditions were applied in all three directions. For long-range electrostatic interactions, particle mesh Ewald (PME) was used. The Coulomb and van der Waals (VdW) cutoff values were set at 1.4 nm. Systems were energy minimized, followed by the equilibration of all the systems for 1 ns. Later, a production run of 5 ns was performed in all three systems along with the 1 ns-short production simulation. The trajectories were analyzed using GROMACS and Python scripts in MDAnalysis suite of programs and visual molecular dynamics (VMD).^{62,63}

For the nonequilibrium molecular dynamic (NEMD) simulation, the SO₃H-rGO filters were placed between the feed side on the left and permeate side on the right, with dimensions of 5 nm × 5 nm × 15 nm in X, Y, and Z directions, respectively. The permeate side consisted of an empty box. For the 0.5 M system, the feed side was filled with 2543 water molecules and 75 Na⁺ and 75 Cl⁻ ions. Similarly, the 1.0 M system contained 2493 water molecules and 151 Na⁺ and 151 Cl⁻ ions. The 1.5 M system consisted of 2443 water molecules and 226 Na⁺ and 226 Cl⁻ ions. A graphene sheet was placed at each end of the simulation box to act as pistons to exert pressure.

■ ASSOCIATED CONTENT

SI Supporting Information

The Supporting Information is available free of charge at <https://pubs.acs.org/doi/10.1021/acssuschemeng.2c04138>.

Ion selectivities of membranes, pore size measurements, powder XRD, SEM-EDS, and tabular performance comparison with previously reported membrane systems (PDF)

■ AUTHOR INFORMATION

Corresponding Authors

Tiju Thomas – Department of Metallurgical and Materials Engineering, Indian Institute of Technology Madras, Chennai 600036, India; Email: tijuthomas@iitm.ac.in

Thalappil Pradeep – International Centre for Clean Water, Chennai 600113, India; DST Unit of Nanoscience, Thematic

Unit of Excellence, Department of Chemistry, Indian Institute of Technology Madras, Chennai 600036, India; orcid.org/0000-0003-3174-534X; Email: pradeep@iitm.ac.in

Authors

Ankit Nagar – DST Unit of Nanoscience, Thematic Unit of Excellence, Department of Chemistry and Department of Metallurgical and Materials Engineering, Indian Institute of Technology Madras, Chennai 600036, India

Md Rabiul Islam – DST Unit of Nanoscience, Thematic Unit of Excellence, Department of Chemistry, Indian Institute of Technology Madras, Chennai 600036, India

Karthek Joshua – DST Unit of Nanoscience, Thematic Unit of Excellence, Department of Chemistry, Indian Institute of Technology Madras, Chennai 600036, India

Tanvi Gupte – DST Unit of Nanoscience, Thematic Unit of Excellence, Department of Chemistry, Indian Institute of Technology Madras, Chennai 600036, India; orcid.org/0000-0002-0518-8482

Sourav Kanti Jana – DST Unit of Nanoscience, Thematic Unit of Excellence, Department of Chemistry, Indian Institute of Technology Madras, Chennai 600036, India; orcid.org/0000-0001-5772-7022

Sujan Manna – DST Unit of Nanoscience, Thematic Unit of Excellence, Department of Chemistry, Indian Institute of Technology Madras, Chennai 600036, India

Complete contact information is available at:

<https://pubs.acs.org/10.1021/acssuschemeng.2c04138>

Notes

The authors declare no competing financial interest.

■ ACKNOWLEDGMENTS

The authors thank the Department of Science and Technology (DST), Government of India, for supporting their research program. A.N., T.G., and S.M. thank IIT Madras for their doctoral student fellowships. M.R.I. thanks the Council of Scientific & Industrial Research (CSIR) for his fellowship.

■ REFERENCES

- (1) Logan, B. E.; Elimelech, M. Membrane-Based Processes for Sustainable Power Generation Using Water. *Nature* **2012**, *488* (7411), 313–319.
- (2) Post, J. W.; Veerman, J.; Hamelers, H. V. M.; Euverink, G. J. W.; Metz, S. J.; Nymeijer, K.; Buisman, C. J. N. Salinity-Gradient Power: Evaluation of Pressure-Retarded Osmosis and Reverse Electrodialysis. *J. Membr. Sci.* **2007**, *288* (1–2), 218–230.
- (3) Porada, S.; Van Egmond, W. J.; Post, J. W.; Saakes, M.; Hamelers, H. V. M. Tailoring Ion Exchange Membranes to Enable Low Osmotic Water Transport and Energy Efficient Electrodialysis. *J. Membr. Sci.* **2018**, *552*, 22–30.
- (4) Hong, J. G.; Gao, H.; Gan, L.; Tong, X.; Xiao, C.; Liu, S.; Zhang, B.; Chen, Y. Nanocomposite and Nanostructured Ion-Exchange Membrane in Salinity Gradient Power Generation Using Reverse Electrodialysis. In *Advanced Nanomaterials for Membrane Synthesis and Its Applications*; Elsevier, 2019; pp 295–316.
- (5) Cusick, R. D.; Kim, Y.; Logan, B. E. Energy Capture from Thermolytic Solutions in Microbial Reverse-Electrodialysis Cells. *Science* (80-). **2012**, *335* (6075), 1474–1477.
- (6) Zhu, X.; Hao, J.; Bao, B.; Zhou, Y.; Zhang, H.; Pang, J.; Jiang, Z.; Jiang, L. Unique Ion Rectification in Hypersaline Environment: A High-Performance and Sustainable Power Generator System. *Sci. Adv.* **2018**, *4* (10), eaau1665.

- (7) Mei, Y.; Liu, L.; Lu, Y.-C.; Tang, C. Y. Reverse Electrodialysis Chemical Cell for Energy Harvesting from Controlled Acid–Base Neutralization. *Environ. Sci. Technol.* **2019**, *53* (8), 4640–4647.
- (8) Siria, A.; Poncharal, P.; Bianco, A.-L.; Fulcrand, R.; Blase, X.; Purcell, S. T.; Bocquet, L. Giant Osmotic Energy Conversion Measured in a Single Transmembrane Boron Nitride Nanotube. *Nature* **2013**, *494* (7438), 455–458.
- (9) Feng, J.; Graf, M.; Liu, K.; Ovchinnikov, D.; Dumcenco, D.; Heiranian, M.; Nandigana, V.; Aluru, N. R.; Kis, A.; Radenovic, A. Single-Layer MoS₂ Nanopores as Nanopower Generators. *Nature* **2016**, *536* (7615), 197–200.
- (10) Macha, M.; Marion, S.; Nandigana, V. V. R.; Radenovic, A. 2D Materials as an Emerging Platform for Nanopore-Based Power Generation. *Nat. Rev. Mater.* **2019**, *4* (9), 588–605.
- (11) Gadaleta, A.; Sempere, C.; Gravelle, S.; Siria, A.; Fulcrand, R.; Ybert, C.; Bocquet, L. Sub-Additive Ionic Transport across Arrays of Solid-State Nanopores. *Phys. Fluids* **2014**, *26* (1), 012005.
- (12) Siria, A.; Bocquet, M.-L.; Bocquet, L. New Avenues for the Large-Scale Harvesting of Blue Energy. *Nat. Rev. Chem.* **2017**, *1* (11), 1–10.
- (13) Ding, L.; Xiao, D.; Lu, Z.; Deng, J.; Wei, Y.; Caro, J.; Wang, H. Oppositely Charged Ti₃C₂T_x MXene Membranes with 2D Nanofluidic Channels for Osmotic Energy Harvesting. *Angew. Chem.* **2020**, *132* (22), 8798–8804.
- (14) Lin, X.; Liu, P.; Xin, W.; Teng, Y.; Chen, J.; Wu, Y.; Zhao, Y.; Kong, X.; Jiang, L.; Wen, L. Heterogeneous MXene/PS-b-P2VP Nanofluidic Membranes with Controllable Ion Transport for Osmotic Energy Conversion. *Adv. Funct. Mater.* **2021**, *31* (45), 2105013.
- (15) Esfandiari, A.; Radha, B.; Wang, F. C.; Yang, Q.; Hu, S.; Garaj, S.; Nair, R. R.; Geim, A. K.; Gopinadhan, K. Size Effect in Ion Transport through Angstrom-Scale Slits. *Science* (80-). **2017**, *358* (6362), 511–513.
- (16) Xiao, K.; Giusto, P.; Wen, L.; Jiang, L.; Antonietti, M. Nanofluidic Ion Transport and Energy Conversion through Ultrathin Free-Standing Polymeric Carbon Nitride Membranes. *Angew. Chemie Int. Ed.* **2018**, *57* (32), 10123–10126.
- (17) Cheng, H.; Zhou, Y.; Feng, Y.; Geng, W.; Liu, Q.; Guo, W.; Jiang, L. Electrokinetic Energy Conversion in Self-Assembled 2D Nanofluidic Channels with Janus Nanobuilding Blocks. *Adv. Mater.* **2017**, *29* (23), 1700177.
- (18) Liu, P.; Sun, Y.; Zhu, C.; Niu, B.; Huang, X.; Kong, X.-Y.; Jiang, L.; Wen, L. Neutralization Reaction Assisted Chemical-Potential-Driven Ion Transport through Layered Titanium Carbides Membrane for Energy Harvesting. *Nano Lett.* **2020**, *20* (5), 3593–3601.
- (19) Xin, W.; Jiang, L.; Wen, L. Two-Dimensional Nanofluidic Membranes toward Harvesting Salinity Gradient Power. *Acc. Chem. Res.* **2021**, *54* (22), 4154–4165.
- (20) Zhang, Z.; Wen, L.; Jiang, L. Nanofluidics for Osmotic Energy Conversion. *Nat. Rev. Mater.* **2021**, *6* (7), 622–639.
- (21) Laucirica, G.; Toimil-Molares, M. E.; Trautmann, C.; Marmisollé, W.; Azzaroni, O. Nanofluidic Osmotic Power Generators—Advanced Nanoporous Membranes and Nanochannels for Blue Energy Harvesting. *Chem. Sci.* **2021**, *12*, 12874.
- (22) Yu, W.; Sisi, L.; Haiyan, Y.; Jie, L. Progress in the Functional Modification of Graphene/Graphene Oxide: A Review. *RSC Adv.* **2020**, *10* (26), 15328–15345.
- (23) Zhou, K.-G.; Vasu, K. S.; Cherian, C. T.; Neek-Amal, M.; Zhang, J. C.; Ghorbanfekr-Kalashami, H.; Huang, K.; Marshall, O. P.; Kravets, V. G.; Abraham, J.; Su, Y.; Grigorenko, A. N.; Pratt, A.; Geim, A. K.; Peeters, F. M.; Novoselov, K. S.; Nair, R. R. Electrically Controlled Water Permeation through Graphene Oxide Membranes. *Nature* **2018**, *559* (7713), 236–240.
- (24) Xue, S.; Ji, C.; Kowal, M. D.; Molas, J. C.; Lin, C.-W.; McVerry, B. T.; Turner, C. L.; Mak, W. H.; Anderson, M.; Muni, M.; Hoek, E. M. V.; Xu, Z.-L.; Kaner, R. B. Nanostructured Graphene Oxide Composite Membranes with Ultrapermeability and Mechanical Robustness. *Nano Lett.* **2020**, *20* (4), 2209–2218.
- (25) Abraham, J.; Vasu, K. S.; Williams, C. D.; Gopinadhan, K.; Su, Y.; Cherian, C. T.; Dix, J.; Prestat, E.; Haigh, S. J.; Grigorieva, I. V.; Carbone, P.; Geim, A. K.; Nair, R. R. Tunable Sieving of Ions Using Graphene Oxide Membranes. *Nat. Nanotechnol.* **2017**, *12* (6), 546.
- (26) Huang, X.; Marsh, K. L.; McVerry, B. T.; Hoek, E. M. V.; Kaner, R. B. Low-Fouling Antibacterial Reverse Osmosis Membranes via Surface Grafting of Graphene Oxide. *ACS Appl. Mater. Interfaces* **2016**, *8* (23), 14334–14338.
- (27) Sanad, M. F.; Chava, V. S. N.; Shalan, A. E.; Enriquez, L. G.; Zheng, T.; Pilla, S.; Sreenivasan, S. T. Engineering of Electron Affinity and Interfacial Charge Transfer of Graphene for Self-Powered Nonenzymatic Biosensor Applications. *ACS Appl. Mater. Interfaces* **2021**, *13* (34), 40731–40741.
- (28) Deng, S.; Gao, E.; Wang, Y.; Sen, S.; Sreenivasan, S. T.; Behura, S.; Král, P.; Xu, Z.; Berry, V. Confined, Oriented, and Electrically Anisotropic Graphene Wrinkles on Bacteria. *ACS Nano* **2016**, *10* (9), 8403–8412.
- (29) Alkhouzaam, A.; Qiblawey, H. Functional GO-Based Membranes for Water Treatment and Desalination: Fabrication Methods, Performance and Advantages. A Review. *Chemosphere* **2021**, *274*, 129853.
- (30) Liu, S.; Yu, J.; Jaroniec, M. Anatase TiO₂ with Dominant High-Energy {001} Facets: Synthesis, Properties, and Applications. *Chem. Mater.* **2011**, *23* (18), 4085–4093.
- (31) Pelaez, M.; Nolan, N. T.; Pillai, S. C.; Seery, M. K.; Falaras, P.; Kontos, A. G.; Dunlop, P. S. M.; Hamilton, J. W. J.; Byrne, J. A.; O’Shea, K.; Entezari, M. H.; Dionysiou, D. D. A Review on the Visible Light Active Titanium Dioxide Photocatalysts for Environmental Applications. *Appl. Catal. B Environ.* **2012**, *125*, 331–349.
- (32) Wang, M.; Jia, Y.; Yao, T.; Wang, K. The Endowment of Monovalent Selectivity to Cation Exchange Membrane by Photo-Induced Covalent Immobilization and Self-Crosslinking of Chitosan. *J. Membr. Sci.* **2013**, *442*, 39–47.
- (33) Islam, M. R.; Gupta, S. S.; Jana, S. K.; Srikrishnarka, P.; Mondal, B.; Chennu, S.; Ahuja, T.; Chakraborty, A.; Pradeep, T. A Covalently Integrated Reduced Graphene Oxide–Ion-Exchange Resin Electrode for Efficient Capacitive Deionization. *Adv. Mater. Interfaces* **2021**, *8* (5), 2001998.
- (34) Luzan, S. M.; Talyzin, A. V. Hydration of Graphite Oxide in Electrolyte and Non-Electrolyte Solutions. *J. Phys. Chem. C* **2011**, *115* (50), 24611–24614.
- (35) Chen, S.; Zhu, J.; Wu, X.; Han, Q.; Wang, X. Graphene Oxide–MnO₂ Nanocomposites for Supercapacitors. *ACS Nano* **2010**, *4* (5), 2822–2830.
- (36) Liu, W.; Cai, J.; Ding, Z.; Li, Z. TiO₂/RGO Composite Aerogels with Controllable and Continuously Tunable Surface Wettability for Varied Aqueous Photocatalysis. *Appl. Catal. B Environ.* **2015**, *174*, 421–426.
- (37) Sher Shah, M. S. A.; Park, A. R.; Zhang, K.; Park, J. H.; Yoo, P. J. Green Synthesis of Biphasic TiO₂–Reduced Graphene Oxide Nanocomposites with Highly Enhanced Photocatalytic Activity. *ACS Appl. Mater. Interfaces* **2012**, *4* (8), 3893–3901.
- (38) Li, Y.; Zhu, H.; Shen, F.; Wan, J.; Lacey, S.; Fang, Z.; Dai, H.; Hu, L. Nanocellulose as Green Dispersant for Two-Dimensional Energy Materials. *Nano energy* **2015**, *13*, 346–354.
- (39) Cote, L. J.; Kim, F.; Huang, J. Langmuir–Blodgett Assembly of Graphite Oxide Single Layers. *J. Am. Chem. Soc.* **2009**, *131* (3), 1043–1049.
- (40) Hafeez, H. Y.; Lakhera, S. K.; Narayanan, N.; Harish, S.; Hayakawa, Y.; Lee, B.-K.; Neppolian, B. Environmentally Sustainable Synthesis of a CoFe₂O₄–TiO₂/RGO Ternary Photocatalyst: A Highly Efficient and Stable Photocatalyst for High Production of Hydrogen (Solar Fuel). *ACS omega* **2019**, *4* (1), 880–891.
- (41) Zhou, S.; Xie, L.; Zhang, L.; Wen, L.; Tang, J.; Zeng, J.; Liu, T.; Peng, D.; Yan, M.; Qiu, B.; Liang, Q.; Liang, K.; Jiang, L.; Kong, B. Interfacial Super-Assembly of Ordered Mesoporous Silica–Alumina Heterostructure Membranes with Ph-Sensitive Properties for Osmotic Energy Harvesting. *ACS Appl. Mater. Interfaces* **2021**, *13* (7), 8782–8793.
- (42) Daiguji, H. Ion Transport in Nanofluidic Channels. *Chem. Soc. Rev.* **2010**, *39* (3), 901–911.

(43) Laucirica, G.; Albesa, A. G.; Toimil-Molares, M. E.; Trautmann, C.; Marmisollé, W. A.; Azzaroni, O. Shape Matters: Enhanced Osmotic Energy Harvesting in Bullet-Shaped Nanochannels. *Nano Energy* **2020**, *71*, 104612.

(44) Yan, F.; Yao, L.; Chen, K.; Yang, Q.; Su, B. An Ultrathin and Highly Porous Silica Nanochannel Membrane: Toward Highly Efficient Salinity Energy Conversion. *J. Mater. Chem. A* **2019**, *7* (5), 2385–2391.

(45) Lu, J.; Zhang, H.; Hou, J.; Li, X.; Hu, X.; Hu, Y.; Easton, C. D.; Li, Q.; Sun, C.; Thornton, A. W.; Hill, M. R.; Zhang, X.; Jiang, G.; Liu, J. Z.; Hill, A. J.; Freeman, B. D.; Jiang, L.; Wang, H. Efficient Metal Ion Sieving in Rectifying Subnanochannels Enabled by Metal–Organic Frameworks. *Nat. Mater.* **2020**, *19* (7), 767–774.

(46) Zhu, C.; Liu, P.; Niu, B.; Liu, Y.; Xin, W.; Chen, W.; Kong, X.-Y.; Zhang, Z.; Jiang, L.; Wen, L. Metallic Two-Dimensional MoS₂ Composites as High-Performance Osmotic Energy Conversion Membranes. *J. Am. Chem. Soc.* **2021**, *143* (4), 1932–1940.

(47) Kamcev, J.; Sujanani, R.; Jang, E.-S.; Yan, N.; Moe, N.; Paul, D. R.; Freeman, B. D. Salt Concentration Dependence of Ionic Conductivity in Ion Exchange Membranes. *J. Membr. Sci.* **2018**, *547*, 123–133.

(48) Xiao, K.; Jiang, L.; Antonietti, M. Ion Transport in Nanofluidic Devices for Energy Harvesting. *Joule* **2019**, *3* (10), 2364–2380.

(49) Pakulski, D.; Czepa, W.; Buffa, S. D.; Ciesielski, A.; Samori, P. Atom-Thick Membranes for Water Purification and Blue Energy Harvesting. *Adv. Funct. Mater.* **2020**, *30* (2), 1902394.

(50) Chen, C.; Liu, D.; He, L.; Qin, S.; Wang, J.; Razal, J. M.; Kotov, N. A.; Lei, W. Bio-Inspired Nanocomposite Membranes for Osmotic Energy Harvesting. *Joule* **2020**, *4* (1), 247–261.

(51) Xin, W.; Xiao, H.; Kong, X.-Y.; Chen, J.; Yang, L.; Niu, B.; Qian, Y.; Teng, Y.; Jiang, L.; Wen, L. Biomimetic Nacre-like Silk-Crosslinked Membranes for Osmotic Energy Harvesting. *ACS Nano* **2020**, *14* (8), 9701–9710.

(52) Pendse, A.; Cetindag, S.; Rehak, P.; Behura, S.; Gao, H.; Nguyen, N. H. L.; Wang, T.; Berry, V.; Kral, P.; Shan, J.; Kim, S. Highly Efficient Osmotic Energy Harvesting in Charged Boron-Nitride-Nanopore Membranes. *Adv. Funct. Mater.* **2021**, *31* (15), 2009586.

(53) Guo, Y.; Ying, Y.; Mao, Y.; Peng, X.; Chen, B. Polystyrene Sulfonate Threaded through a Metal–Organic Framework Membrane for Fast and Selective Lithium-ion Separation. *Angew. Chem.* **2016**, *128* (48), 15344–15348.

(54) Wang, F.; Wang, Z.; Wang, S.; Meng, X.; Jin, Y.; Yang, N.; Sunarso, J.; Liu, S. Mechanically Intensified and Stabilized MXene Membranes via the Combination of Graphene Oxide for Highly Efficient Osmotic Power Production. *J. Membr. Sci.* **2022**, *647*, 120280.

(55) Xu, Y.; Zhang, K.; Chen, S.; Zhang, X.; Chen, Y.; Li, D.; Xu, F. Two-Dimensional Lamellar MXene/Three-Dimensional Network Bacterial Nanocellulose Nanofiber Composite Janus Membranes as Nanofluidic Osmotic Power Generators. *Electrochim. Acta* **2022**, *412*, 140162.

(56) Liu, Y.-C.; Yeh, L.-H.; Zheng, M.-J.; Wu, K. C.-W. Highly Selective and High-Performance Osmotic Power Generators in Subnanochannel Membranes Enabled by Metal–Organic Frameworks. *Sci. Adv.* **2021**, *7* (10), eabe9924.

(57) Muraru, S.; Burns, J. S.; Ionita, M. GOPY: A Tool for Building 2D Graphene-Based Computational Models. *SoftwareX* **2020**, *12*, 100586.

(58) Baweja, L.; Balamurugan, K.; Subramanian, V.; Dhawan, A. Hydration Patterns of Graphene-Based Nanomaterials (GBNMs) Play a Major Role in the Stability of a Helical Protein: A Molecular Dynamics Simulation Study. *Langmuir* **2013**, *29* (46), 14230–14238.

(59) Wang, J.; Wolf, R. M.; Caldwell, J. W.; Kollman, P. A.; Case, D. A. Development and Testing of a General Amber Force Field. *J. Comput. Chem.* **2004**, *25* (9), 1157–1174.

(60) Bayly, C. I.; Cieplak, P.; Cornell, W.; Kollman, P. A. A Well-Behaved Electrostatic Potential Based Method Using Charge

Restrains for Deriving Atomic Charges: The RESP Model. *J. Phys. Chem.* **1993**, *97* (40), 10269–10280.

(61) Jakalian, A.; Bush, B. L.; Jack, D. B.; Bayly, C. I. Fast, Efficient Generation of High-quality Atomic Charges. AM1-BCC Model: I. Method. *J. Comput. Chem.* **2000**, *21* (2), 132–146.

(62) Abraham, M. J.; Murtola, T.; Schulz, R.; Páll, S.; Smith, J. C.; Hess, B.; Lindahl, E. GROMACS: High Performance Molecular Simulations through Multi-Level Parallelism from Laptops to Supercomputers. *SoftwareX* **2015**, *1*, 19–25.

(63) Humphrey, W.; Dalke, A.; Schulten, K. VMD: Visual Molecular Dynamics. *J. Mol. Graph.* **1996**, *14* (1), 33–38.

Recommended by ACS

Improving the Performance of the Lamellar Reduced Graphene Oxide/Molybdenum Sulfide Nanofiltration Membrane through Accelerated Water-Transport Chan...

Jiajian Xing, Xie Quan, *et al.*

DECEMBER 16, 2022

ENVIRONMENTAL SCIENCE & TECHNOLOGY

READ 

Functionalized Graphene Oxide-Based Lamellar Membranes with Tunable Nanochannels for Ionic and Molecular Separation

Akbar Ali, Khalid Hussain Thebo, *et al.*

AUGUST 31, 2022

ACS OMEGA

READ 

Interfacial Ions Sieving for Ultrafast and Complete Desalination through 2D Nanochannel Defined Graphene Composite Membranes

Dian Gong, Gaofeng Zeng, *et al.*

JUNE 11, 2021

ACS NANO

READ 

A Facile and Scalable Method of Fabrication of Large-Area Ultrathin Graphene Oxide Nanofiltration Membrane

Zhiyu Liu, John H. Xin, *et al.*

SEPTEMBER 03, 2021

ACS NANO

READ 

Get More Suggestions >